Journal of Electroceramics, 12, 119–131, 2004


# Science and Technology of High Dielectric Constant Thin Films and Materials Integration for Application to High Frequency Devices

O. AUCIELLO, S. SAHA, D.Y. KAUFMAN, S.K. STREIFFER, W. FAN, B. KABIUS, J. IM* & P. BAUMANN†

*Argonne National Laboratory, Materials Science Division, 9700 South Cass Ave, Argonne, IL-60439, USA*

**Abstract.** Thin films of $Ba_{1-x}Sr_xTi_{1+y}O_{3+z}$ (BST), were fabricated using both by RF-magnetron sputtering and MOCVD to demonstrate application to high frequency devices. Precise control of composition and microstructure is critical for the production of $(Ba_xSr_{1-x})Ti_{1+y}O_{3+z}$ (BST) dielectric thin films with the large dependence of permittivity on electric field, low losses, and high electrical breakdown fields that are required for successful integration of BST into tunable high frequency devices. Here we review results on composition-microstructure-electrical property relationships of polycrystalline BST films produced by magnetron sputter deposition that are appropriate for microwave devices such as phase shifters. BST films with a multilayer structure were also developed with different Ti-elemental ratio in each layer to minimize losses and leakage current. Interfacial contamination from C and H species was studied and implications on electrical properties are highlighted. Finally, York's group at the University of California-Santa Barbara successfully integrated our BST films onto phase shifter arrays. The results show potential of BST films in such applications. Results from initial work on the integration of Cu-electrodes with BST films are also presented.

**Keywords:** high dielectric constant, thin films, high-frequency devices

## 1. Introduction

It is well known that nonlinear dielectrics such as $Ba_{1-x}Sr_xTi_{1+y}O_{3+z}$ (BST), exhibit large variation in permittivity, $\varepsilon$, as a function of the electric field applied to the material. Therefore, BST is a suitable candidate for high-frequency voltage-tunable microwave devices such as resonators, filters, and phase-shifters [1–4]. For these applications it is desirable to produce BST thin films, which have maximum tunability with a minimum loss factor. A theoretical parameter, $K$ (figure of merit) can be defined to reflect the quality of the film in terms of tunability and loss as:

$$K = \frac{\left\lfloor \%\,\text{tunability} \equiv \frac{\varepsilon_{\max}-\varepsilon_{\min}}{\varepsilon_{\max}} \right\rfloor}{\tan\delta(\%)} \qquad (1)$$

where $\varepsilon_{\max}$, $\varepsilon_{\min}$ are the maximum and minimum dielectric permittivity, respectively, over the investigated voltage range, and the dissipation factor ($\tan\delta$) given as a percentage. The relationship (1) shows how the loss factor along with the tunability contributes to the device performance. In order to obtain high $K$ values it becomes necessary to understand the composition-microstructure-electrical property relationships of polycrystalline BST thin films. We have performed extensive studies of issues such as the effect of composition, thin film deposition parameters, electrode influence on the electrical properties of BST thin films in order to understand composition-microstructure-property relationships. Different levels of optimization are highlighted in each section that show how carefully chosen parameters result in film property improvement in each stage.

As part of the process optimization for integration of BST films into high frequency devices, we studied properties of BST solid solution films deposited by rf-magnetron sputtering, MOCVD, and the fabrication of BST capacitors based on Cu-electrodes. RF-magnetron sputtering provided easy control of stoichiometry while MOCVD BST films provided superior

*Present address: Agere Systems, Wafer Fab R&D, Alhambra, CA.
†Present address: Aixtron, Aachen, Germany.

composition control and conformal coverage of device structures. Along with growth issues, we have addressed the effects of surface contamination on the BST electrical properties. In this review we report results from our extensive research program focused on integrating thin film BST into current microwave technology. We also highlight results from our collaborative work with York et al. of UCSB, whose group used our BST films to fabricate phase-shifters based on their circuit design in order to demonstrate the viability of BST thin film technology for use in microwave circuits.

## 2. Synthesis and Characterization of $Ba_{1-x}Sr_xTi_{1+y}O_{3+z}$ Thin Films by RF-Magnetron Sputtering

### *2.1.A. Synthesis of BST Solid-Solution Films*

$Ba_{1-x}Sr_xTi_{1+y}O_{3+z}$ thin films were synthesized using RF-magnetron sputtering in Ar-$O_2$ gas mixtures [5]. The substrate and target (a sintered stoichiometric $Ba_{0.5}Sr_{0.5}TiO_3$ disc) were positioned parallel to each other in an on-axis configuration with 10 cm separation. BST films were deposited at 650°C on Pt(120 nm)/$TiO_2$(40 nm)/$SiO_2$(300 nm)/Si or Pt(100 nm)/$SiO_2$(300 nm)/Si substrates. High resistivity silicon (>10 kΩ-cm) substrates were also used in anticipation of microwave circuit applications.

Patterned Pt top electrodes were deposited through a shadow mask onto the BST films at 350°C, using electron beam evaporation. Subsequent to top electrode deposition, samples were annealed in air at 550°C for 30 min. This was followed by a 700°C anneal for 60 min, to improve the structure and chemistry of both the bulk BST film and the top electrode/BST interface, with the aim of reducing bulk and interfacial contributions to the dielectric loss tangent. RBS, XRD, field emission SEM (FESEM), and atomic force microscopy AFM were used to investigate the thickness, composition, crystallographic orientation, microstructure, and roughness of the BST films, respectively. Dielectric properties (relative permittivity, $\varepsilon$ and dielectric loss, $\tan\delta$ were measured as a function of applied electric field at 10 kHz and 0.1 $V_{rms}$. oscillation level, using a HP 4192A impedance analyzer. Capacitance and loss were also characterized at 1 MHz using a Keithley C-V meter. Leakage current was measured using a Keithley SMU 237 measurement unit.

### *2.1.B. Synthesis of BST Multilayered Structure*

BST multilayer structures were fabricated using RF-magnetron sputtering in Ar-$O_2$ gas mixtures with the same geometry as mentioned above. First, a thin BST layer (∼5 nm) with a (Ba + Sr)/Ti ratio of 0.73 was deposited at room temperature on top of the Pt bottom electrode. A low temperature (room temperature) BST film deposition process for the initial layer improved the device yields of BST capacitors, presumably by reducing roughening and hillocking of the Pt [6]. Subsequently, a 60 nm main BST layer with a (Ba + Sr)/Ti ratio of 0.9 was deposited at 650°C onto the initial layer. Finally, another Ti-rich [∼5 nm, (Ba + Sr)/Ti = 0.73] BST interfacial layer was deposited onto the heterostructure at 650°C. All three BST layers were deposited without breaking vacuum, using a single ceramic stoichiometric $Ba_{0.5}Sr_{0.5}TiO_3$ target. Different compositions and microstructures for the layers were achieved by changing the total process gas (Ar+$O_2$) pressure, which affects the relative incident fluxes of the Ba, Sr, and Ti species via gas-phase collisions [7].

### *2.2. Composition Control and Physical Properties*

Figure 1(a) shows the variation of the (Ba + Sr)/Ti and Ba/Sr ratios in BST films as a function of the total (Ar+$O_2$) deposition pressure with the $O_2$/Ar ratio fixed at 1/5. The ratio of (Ba + Sr)/Ti changed from 0.73 to 0.98 for films grown with total gas pressure from 22 to 58 mTorr. The growth rate of the BST films depends on the total process pressure (Fig. 1(b)). Variation of the $O_2$/Ar ratio in the 1:1–1:5 range did not affect the metallic composition of the BST films.

BST films with (Ba + Sr)/Ti ratios ≥0.9 exhibited a polycrystalline structure characterized by (100), (110), and (111) peaks in the XRD spectra [7], which disappeared for (Ba + Sr)/Ti ratios below 0.85 [7]. This, coupled with the relatively high permittivities still found for these samples, suggests that high-Ti BST films are nanocrystalline, BST films with (Ba + Sr)/Ti ratios >0.9 exhibited a dense and granular microstructure, while BST films with (Ba + Sr)/Ti ratios <0.85 exhibited a featureless microstructure. The root-mean-square (rms) roughness measured by APM was approximately 3 nm for BST films with (Ba + Sr)/Ti ≥ 0.9 and 2 nm for BST films with (Ba + Sr)/Ti ≤ 0.85, correlating with the structural changes indicated by XRD spectra.

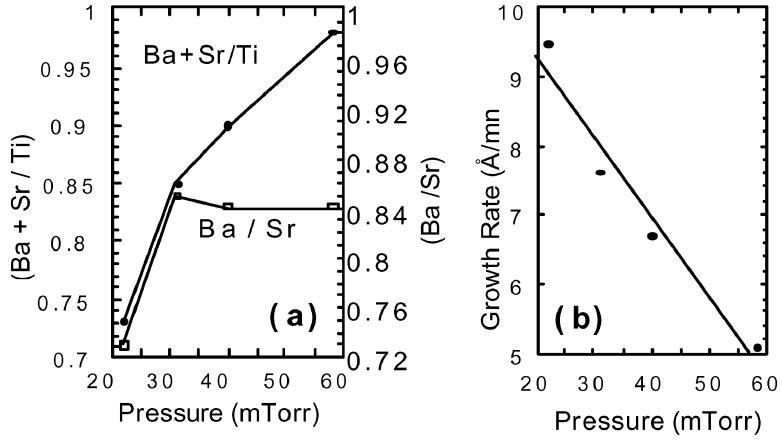


*Fig. 1.* (a) Variation of (Ba + Sr)/Ti and Ba/Sr ratios for BST films deposited at 650°C from a stoichiometric target with a Ba/Sr ratio of 50/50, and (b) growth rate as a function of the total pressure ($Ar + O_2$) [7].

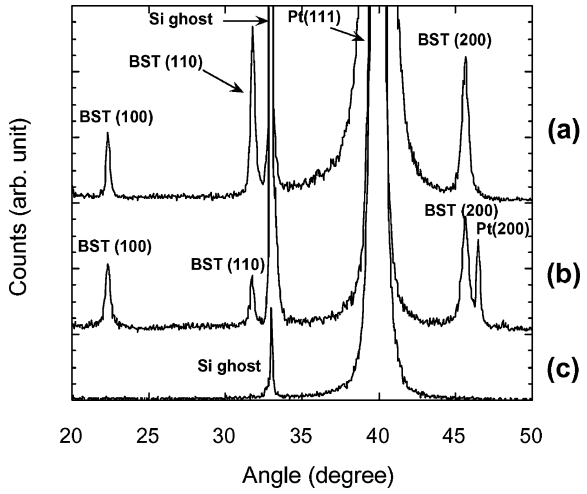


*Fig. 2.* XRD spectra of BST films without (a) and with (b) (Ba + Sr)/Ti = 0.73 interfacial layers. (c) XRD spectrum of a BST film with a (Ba + Sr)/Ti = 0.73 composition.

For multilayered BST films, the X-ray diffraction spectra with interfacial layers are shown in Fig. 2. The XRD spectrum for the layered BST film including the interfacial layers shows a general decrease in the intensity of the BST peaks and a change in the relative intensities of the (100) and (110) peaks (Fig. 2(b)). An XRD spectrum of a BST film with the same composition as the Ti-rich interfacial layers is shown in Fig. 2(c), as a reference. Although transmission electron microscopy would be necessary to confirm this hypothesis, the absence of diffraction peaks from the XRD spectrum of the Ti-rich layer is indicative that the layer is likely nanocrystalline, as an amorphous film would show negligible tunability, which is not the case as described latter on this paper. The reduction in the BST peaks intensity of the layered BST film can be interpreted as an indication that the Ti-rich interfacial layer reduces the overall crystallinity of the layered BST film.

### 2.3. *Electrical Properties*

In Fig. 3 curves (a) and (d) shows the field-dependent dielectric properties of a single 70 nm BST layer ((Ba + Sr)/Ti = 0.90). This capacitor exhibited zero-bias permittivity of 480, 72% tunability at breakdown, and a dielectric loss $\tan\delta = 0.013$ at zero bias and room temperature. The $K$ value was calculated as 55. In comparison, a BST capacitors with a Ti-rich composition [(Ba + Sr)/Ti ratio of 0.73] showed zero-bias permittivity of 170, 47% tunability and a dielectric loss $\tan\delta = 0.0047$ (curves (c) and (f) in Fig. 3) at zero bias, which yielded a $K$ value of 100. Improvement in the multilayer structure is shown in Fig. 3, curves (b) and (e), the field-dependent dielectric properties of a BST capacitor with a (Ba + Sr)/Ti = 0.90 BST layer sandwiched between two (Ba + Sr)/Ti = 0.73 BST interfacial layers. This heterostructure exhibited low loss, almost identical to that of the interfacial BST layer itself (∼0.005) at zero bias and room temperature, yet maintained an intermediate zero-bias permittivity of 270, and high tunability (76%) of the

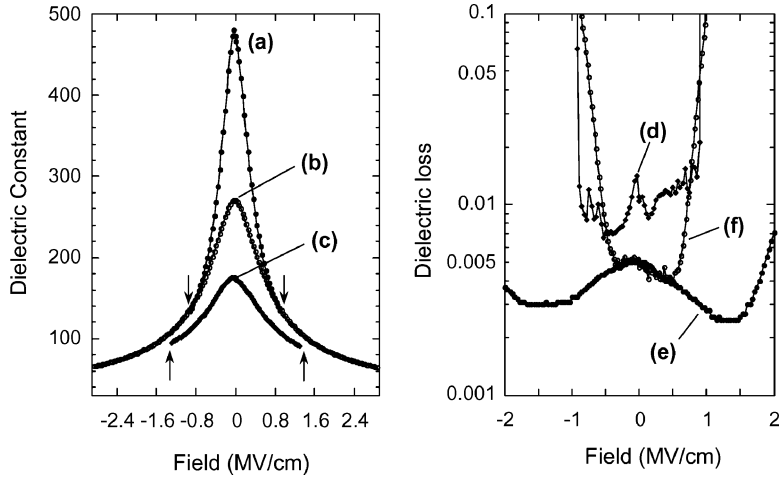


*Fig. 3.* Permittivity of BST films without (a) and with (b) (Ba + Sr)/Ti = 0.73 interfacial layers. (c) Permittivity of a BST film with (Ba + Sr)/Ti = 0.73. Also, dielectric loss of BST films without (d) and with (e) (Ba + Sr)/Ti = 0.73 interfacial layers. (f) dielectric loss of a BST film with (Ba + Sr)/Ti = 0.73. The arrows in Fig. 3(a) and (c) indicate the breakdown field of the BST films.

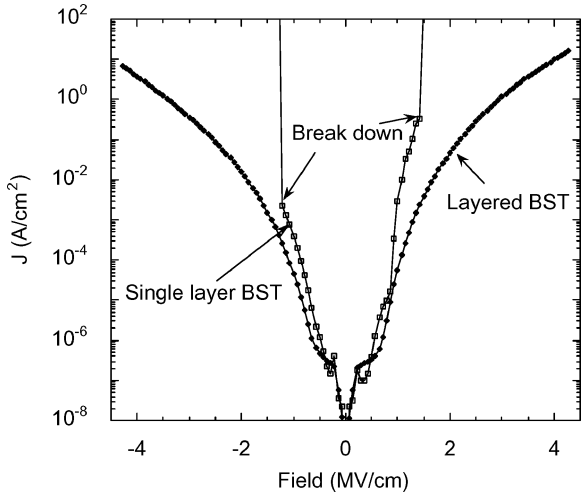


*Fig. 4.* Leakage current density vs. electric field curves for a capacitor with Pt/(Ba + Sr)/Ti = 0.73/(Ba + Sr)/Ti = 0.9/(Ba + Sr)/Ti = 0.73/Pt layered structure and a capacitor with a single layer BST ((Ba + Sr)/Ti = 0.9).

primary BST layer, corresponding to a $K$ value of 150.

The data presented in Fig. 4 indicate that a single layer near-stoichiometric BST film exhibited a breakdown field of ∼1 MV/cm (see arrows in Fig. 3 curves (a) and (c)). On the other hand, BST capacitors with bottom and top (Ba + Sr)/Ti = 0.73 interfacial layers exhibited substantially improved breakdown fields up to ∼4 MV/cm, as shown in dependence of leakage current on applied field (Fig. 4). The mean breakdown field is 4.2 MV/cm with a standard deviation of 0.2, resulting from measurements on 10 layered BST capacitors. This increase in breakdown field results in a tunability comparable to that of the near-stoichiometric single layer film, despite some reduction in zero-bias permittivity.

## 3. Synthesis and Characterization of MOCVD $Ba_{1-x}Sr_xTi_{1+y}O_{3+z}$ Thin Films

### *3.1. Synthesis*

In the second approach $Ba_{1-x}Sr_xTi_{1+y}O_{3+z}$ thin films were fabricated using a large area vertical MOCVD system. Metalorganic precursors of $Ba(thd)_2$, $Sr(thd)_2$, and $Ti(O\text{-}iPr)_2\text{-}(thd)_2$ with polyamine adducts were introduced using high purity nitrogen as a carrier gas into the MOCVD reactor, via a temperature-controlled flash-vaporizer and a computer-controlled liquid delivery system (ATMI LDS-300B) that provides good composition control and reproducibility of the delivered precursor mixture. The temperatures of the delivery lines were controlled to avoid condensation or premature reaction of the precursors prior to introduction into the MOCVD reactor. The precursors were thoroughly mixed with high purity reactive gases ($O_2$ and $N_2$) in a showerhead designed to provide deposition

*Table 1*. Deposition and processing parameters for MOCVD synthesis of BST thin films

| | |
|---|---|
| Substrates | Pt (1000 Å)/$SiO_2$(1000 Å)/Si |
| Substrate heater temperature | 650°C |
| Reactive gases | $O_2$ and $N_2O$ |
| Reactive gas flow rate | 250–1000 SCCM |
| Reactor pressure | 1.5–2.7 Torr |
| Top electrodes | e-beam evaporated Pt(1000 Å) |
| Post electrode anneal | 550°C for 0.5 hrs |
| Electrical characterization | HP4192A at 1 MHz and 0.1 V rms |

of BST films with uniform composition and thickness over large area substrates. The film deposition and processing conditions are summarized in Table 1. The (Ba + Sr)/Ti ratios were varied between 0.96 and 1.05 while the Ba/Sr ratio of the BST thin films was kept at 70/30. Further details of the deposition system have been reported previously [8]. We report the properties of BST films deposited in a thickness range of 90 to 480 nm.

### 3.2. *Microstructure and Crystallinitiy of BST Films*

$Ba_{1-x}Sr_xTi_{1+y}O_{3+z}$ thin films deposited by MOCVD are polycrystalline and show a highly (100) oriented growth. Figure 5(a) shows the x-ray diffraction pattern of a BST film grown at 675°C with a (Ba + Sr)/Ti ratio of 0.93, while Fig. 5(b) shows a SEM picture revealing the grain structure of the BST film. Films grown with a total reactive gas flow rate of 750 sccm exhibited strong (100) fiber texture. Excellent film uniformity was obtained over a 4-inch wafer. Initial growth rates were ≈12 Å/min, but higher rates of ≈50 Å/min were achieved after optimization of the reactor showerhead configuration and vaporizer temperature uniformity (±5°C). It is well-established that the electrical properties of BST film-based capacitors depend on the (Ba + Sr)/Ti ratio [7–10]. Slightly Ti rich samples with (Ba + Sr)/Ti about 0.96 were studied here. A broader range of (Ba + Sr)/Ti ratios is still under investigation.

### 3.3. *Electrical Properties*

Figure 6 shows the room temperature relative permittivity vs. electric field characteristics as a function of BST film thickness. The zero-field dielectric constant increases systematically with increasing film thickness, while at higher fields, the permittivities become thickness independent, as consistent with previous observations [1, 11]. Losses for all samples were less than 0.5% at room temperature and zero bias.

Figure 7 shows the leakage current characteristics of a 90 nm BST film as a function of temperature and applied electric field. The leakage current behavior can be divided into low-field and high-field regimes. The low-field regime is characterized by weak field dependence and a monotonic increase in leakage with increasing temperature. The high-field regime, in contrast, shows a strong dependence on applied electric field, and a distinct crossover point beyond which the leakage current is found to decrease with increasing temperature.

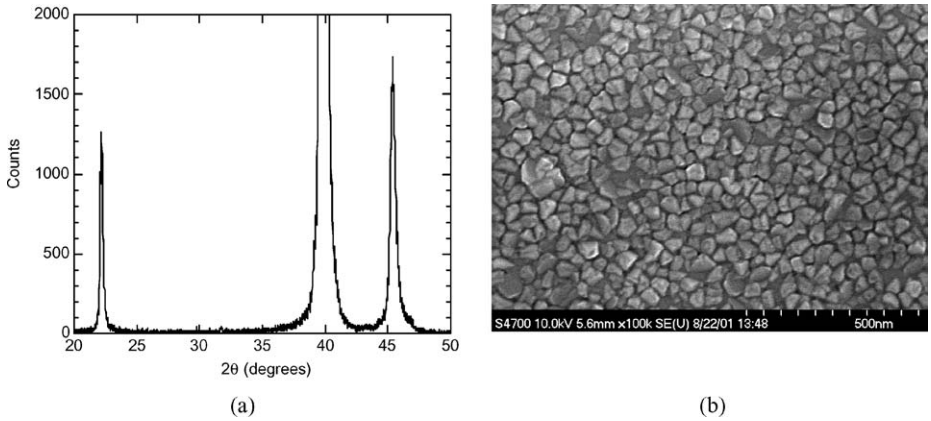


(a) (b)

*Fig. 5*. (a) XRD spectrum of a BST film grown by MOCVD at 675°C with a (Ba + Sr)/Ti = 0.93. (b) SEM picture showing the microstructure of the BST film which XRD is shown in (a).

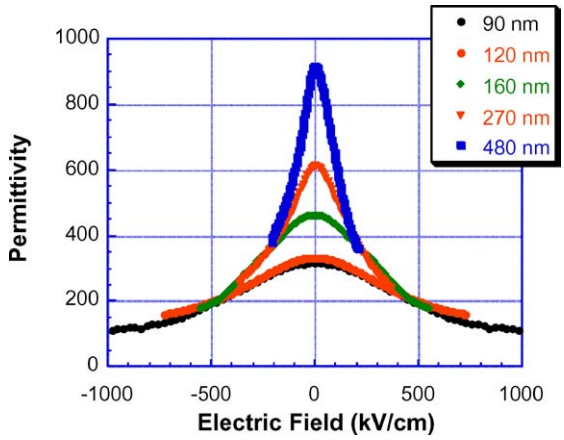


*Fig. 6.* Relative permittivity vs. electric field characteristics as a function of BST film thickness.

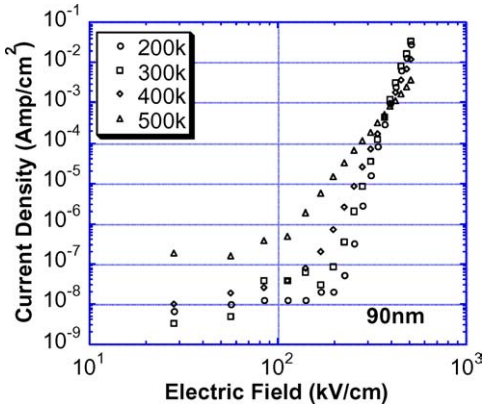


*Fig. 7.* Leakage current characteristics of a 90 nm BST film as a function of temperature and applied electric field.

A detailed analysis of the leakage characteristics can be found elsewhere [12].

## 4. $(Ba_xSr_{1-x})Ti_{1+y}O_{3+z}$ Interface Contamination and its Effect on Electrical Properties

In order to fabricate high quality BST/electrode heterostructures for such devices, it is important to understand the effect of contamination at the film-electrode interfaces. For example, carbon- and hydrogen-containing contaminants at interfaces are generally known to affect the Schottky barrier height, which may be one of contributing factors to leakage current of BST capacitors. Hydrocarbon contaminants are generally adsorbed on the surface of BST layers or metal electrodes when substrates are transported through air from one growth chamber to another in a research environment. This problem should be overcome in an industrial environment where it is expected that the fabrication of BST capacitors will be done in integrated cycles without exposing the capacitors layers to air. In any case, we performed systematic studies on the extent of contamination of the surfaces of BST and Pt thin films using *in-situ*, real time mass spectroscopy of recoiled ions (MSRI), coupled with thermal decomposition/desorption in an oxygen ambient for the cleaning of the surfaces. Surface compositional analysis was performed using the MSRI technique, which permits compositional analysis of the top surface layer ($<3$ monolayers) of thin films in backfill sputtering and reactive gas environments.

Figure 8(a) shows the result from *in situ*, real-time MSRI analysis performed during heating of BST films in vacuum or oxygen atmospheres up to 700°C, in order to determine the conditions that result in the elimination of C and H species from the surface of the BST film. Complete removal of C and H species from the surface of BST films was accomplished only when heating the films at $\geq$550°C in $\geq$1 mTorr of oxygen 5 min [13, 14], which indicates that the oxygen atmosphere is particularly critical for achieving a clean BST film surface prior to top electrode deposition. The elimination of C and H species from the BST surface is due to chemical reactions between oxygen and C and H species that result in the formation of volatile CO and/or $CO_2$ and $H_2O$ molecules activated by the high substrate temperature. A gradual decrease in surface contamination is observed at low $O_2$ pressure (0.5 mTorr and vacuum) over the entire temperature range studied. In contrast, upon heating in 1 mTorr of oxygen, the magnitude of the carbon peak starts to decrease above about 400°C (Fig. 8(a)), while the magnitude of the hydrogen peak starts to decrease above 300°C (Fig. 8(b)); both fall below the limits of detectability between 500 and 550°C.

The effect of C and H contamination on the electrical properties can be observed in the leakage properties shown in Fig. 9(a) and (b). Before the standard post-capacitor fabrication anneal, a strong polarity dependence is observed in the leakage of the capacitor with top electrodes deposited at 350°C in vacuum and therefore with top interface contamination, compared to the sample with Pt electrodes deposited under optimized conditions yielding a clean top interface (Fig. 9(a)).

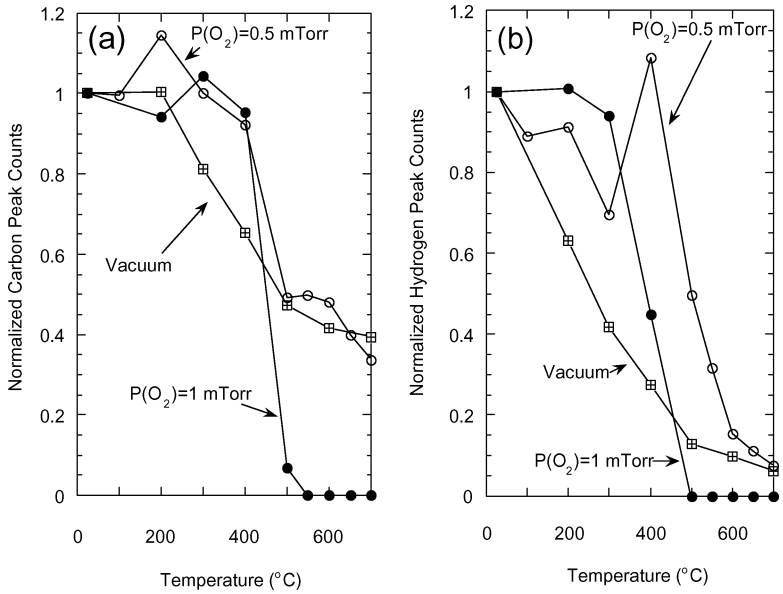


*Fig. 8.* MSRI peak count evolution for (a) carbon and (b) hydrogen during heating of BST films in vacuum and in oxygen ambient of $5 \times 10^{-4}$ Torr and $1 \times 10^{-3}$ Torr, respectively.

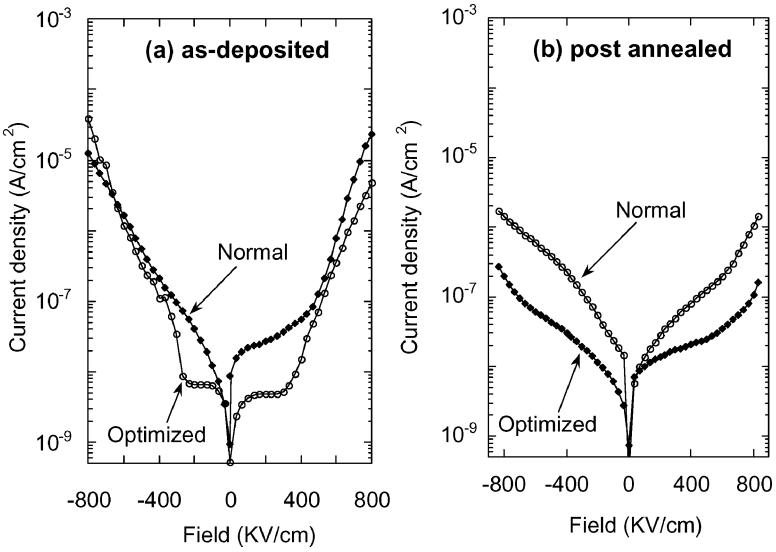


*Fig. 9.* Current density vs. electric field for Pt/60 nm BST/Pt heterostructures with Pt top electrodes deposited either at 350°C in vacuum (marked as "normal") or deposited under conditions yielding a clean top interface (marked as "optimized"), for (a) as-deposited electrodes and (b) after annealing in air for 30 minutes at 550°C.

It is important to notice that the vacuum achieved in non-ultrahigh vacuum deposition systems, including ours, used to produce electrode layers, is in the range of $10^{-6}$–$10^{-8}$ Torr. Under these vacuum conditions, C and H species from the background gas re-adsorb on the film surface quickly if the latter is cooled down below the 500°C range. This can be observed if the system has a suitable surface analytical technique such as our MSRI method capable of monolayer analysis resolution. Therefore, in order to produce a clean Pt/BST

interface, we annealed the BST film in 1 mTorr at 550°C, and then deposited the first 50 Å of Pt under these same condition. This was followed by deposition of the remaining top Pt electrode (950 Å) at 350°C in vacuum. In view of the BST processing described above, the asymmetric leakage, observed also in BST capacitors with the top Pt electrode deposited at 350°C in vacuum, can be correlated with differences in the behavior of the top and bottom electrode interfaces, and therefore to some degree to the presence of C and H contaminants at the top Pt/BST interface. In addition, BST capacitors with top Pt electrodes deposited under the optimized conditions shown in Fig. 8, and therefore with clean top and bottom interfaces, exhibited almost no polarity dependence (Fig. 9(a)) and reduced dielectric loss (0.012) but similar capacitance, compared to BST capacitors with Pt top electrode deposited at 350°C (dielectric loss = ∼0.02).

The conclusions presented above are reinforced by the behavior of BST capacitors after annealing of the whole Pt/BST/Pt capacitors at 550°C in air, following top Pt electrode deposition at 350°C in vacuum. Figure 9(b) shows the leakage current densities after annealing of the as-fabricated capacitors, at 550°C for 30 minutes in air. Substantial reduction and a relatively symmetric behavior of the leakage are found for BST capacitor fabricated both with the optimized top Pt electrode process and the standard top Pt process [13, 14]. After the post-capacitor fabrication anneal, both BST capacitors show similar values of the dielectric loss (∼0.01).

## 5. Phase Shifters Based on Optimized Magnetron Sputter-Deposited BST Films

Optimized BST thin films described above have been incorporated into monolithic microwave integrated capacitors in thin-film phase-shifters circuits in work performed by York et al. based on their unique devise design [15, 16]. The approach taken by York's group work was to fabricate monolithic parallel-plate capacitors using standard IC processes, and integrate these with microwave coplanar-waveguide transmission-line structures. Figure 10 illustrates a simple parallel-plate capacitor structure integrated in shunt along a coplanar transmission-line (CPW) (a), an array of capacitors loading a transmission line (b), and a typical

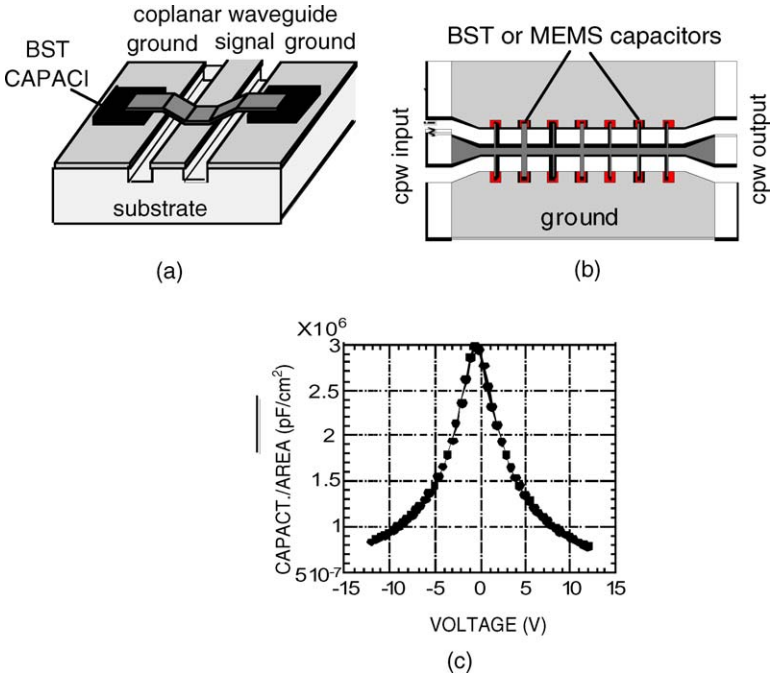


*Fig. 10.* (a) Integrated thin-film capacitor structure on a coplanar waveguide, (b) distributed circuit phase shifter using a periodically-loaded coplanar waveguide and (c). Low-frequency (1 MHz) C–V curve of a typical UCSB /ANL device showing 4:1 capacitance.

capacitance vs. voltage curve (c) for the device fabricated at UCSB using BST films produced at Argonne. For lowest possible loss, the silicon substrates can be micromachined in the CPW gap region as shown in Fig. 10(b). This also has the advantage of reducing the capacitance per unit length on the unloaded-line, allowing for larger capacitive loading in a circuit.

The monolithic delay lines shown in Fig. 10(b) are distributed circuits using a coplanar waveguide periodically loaded with thin-film BST varactors. When designed correctly, this structure is a synthetic transmission line with a phase velocity that can be controlled by changing the value of the external loading capacitors. The parallel plate capacitor topology utilizes the tunability of the BST film effectively and requires lower control voltages than interdigitated electrode designs. Conductor losses are low in this topology.

York et al. have recently used this topology to demonstrate analog phase shifter circuits using monolithic GaAs varactors loading a coplanar waveguide (CPW) transmission line in K-band, resulting in <4 dB insertion loss at 20 GHz and a continuously programmable delay of 0–360 degrees at this frequency [15, 16]. Excellent performance of the phase shifters was the result of careful modeling of the circuit, especially with respect to RF losses, which enabled the optimization of the structure for low insertion loss and high performance. An especially important parameter is the loading factor 'x', which is the ratio of the variable capacitor per unit length to the unloaded line capacitance per unit length. For a given variable capacitor technology and substrate dielectric constant there exists an optimum-loading factor, which results in a circuit with the lowest possible insertion loss. This has been experimentally verified by measuring the losses on GaAs varactor loaded transmission lines, and it was found that losses for the optimally loaded transmission line are dominated by the losses in the variable capacitor. Thus, further efforts to reduce the losses of the circuit must concentrate on reducing losses in the variable capacitor, which favors the use of thin-film BST technology.

To demonstrate the potential of BST thin film varactors for distributed phase-shifters, a loss analysis was carried out by York's group for different substrate dielectric constants and for different values of loss tangent of the BST film. The results are displayed in Fig. 11(a), which shows that there is a certain optimum loading factor for minimization of the total circuit loss. The total circuit loss decreases with a decrease in the

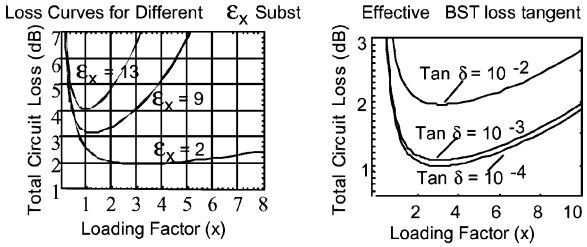


*Fig. 11.* Predicted losses for BST-based circuits like that of Fig. 11. (a) Influence of substrate dielectric constant ($\tan\delta = 0.02$, or $Q = 50$); and (b) Influence of loss tangent ($\varepsilon_r = 2$).

substrate dielectric constant, due to a subtle interplay between conductor loss and characteristic impedance. Since the BST technology enables the use of different substrates, it should be possible to achieve substantially lower loss than with GaAs-based circuits. Another set of calculations performed by York's group was to determine the effect of the BST thin film loss tangents on the total phase shifter losses as shown in Fig. 11(b). At loss tangents of $10^{-3}$ or lower (specified at 10 GHz) the performance is limited by conductor loss only, indicating that significant improvements over diode-based circuits can be obtained with material improvements, particularly on electrode materials once the BST material has been fully optimized.

York et al. have recently demonstrated a BST-based periodically loaded line phase shifter [17] as shown in Fig. 10(b). The phase shifter was capable of producing up to 160° of phase shift at 30 GHz. The phase shift increases linearly with frequency as expected for a variable time delay element. The preliminary results of this phase shifter are shown in Fig. 12. Although this phase shifter has not yet been fully optimized, the results confirm the potential of thin film BST technology for application to high frequency devices. Advances in materials and materials integration strategies are required to further improve on these results, particularly on electrode materials, which is the topic of the next section.

## 6. Synthesis and Properties of $(Ba_xSr_{1-x})TiO_3$ Thin Film Capacitors with Layered Cu-Based Electrode

Copper has drawn much attention [18, 19] as an interconnect material for integrated sub-micron circuit

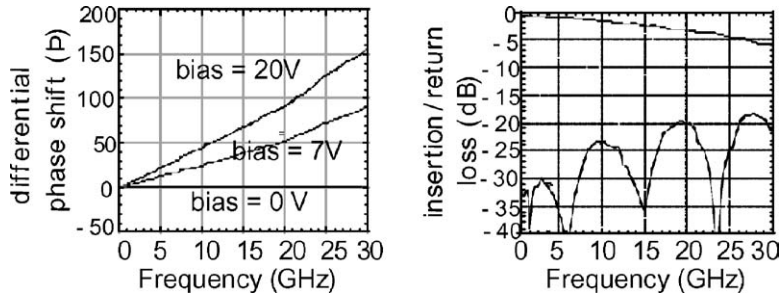


*Fig. 12.* Measured performance of a periodically loaded line phase shifter fabricated at UCSB.

technology due to its low resistivity and high electro- and stress-migration resistance, which are superior to that of Al and Al-alloy-based IC interconnection technologies, and this is the reason why Cu has now been introduced into IC fabrication. In addition, compared to Pt (widely used as the electrode material in ferroelectric and complex oxide thin film devices), copper's low cost, high conductivity, and relatively easy reactive ion etching properties, makes it an appealing candidate to replace Pt for non-volatile ferroelectric memories and other ferroelectric and complex oxide thin film-based devices. However, there are several issues to be solved before Cu can be successfully integrated as an electrode for oxide thin films. We have developed layered structures of TiAl/Cu/Ta to solve the Cu diffusion, adhesion, and oxidation problem encountered in the fabrication of high-k thin film-based capacitors for application to high frequency devices [20]. Tantalum (Ta) has been extensively investigated and demonstrated to be an excellent diffusion barrier for Cu integration with $SiO_2$/Si substrates [21, 22], due to its high melting temperature and thermodynamic stability with respect to Cu and Si. The TiAl layer, working as oxygen diffusion barrier, exhibits very good barrier properties against oxygen penetration at elevated temperature [23, 24]. Polycrystalline $(Ba_xSr_{1-x})TiO_3$ (BST) thin films, which is a high-dielectric oxide material, were subsequently grown on the Cu-based electrode as discussed in our prior publication [20].

### *6.1. Synthesis of Cu-Based Electrodes*

Stacked layers of TiAl(20–50 nm)/Cu(100–200 nm)/Ta(20 nm) were produced on thermally oxidized Si(100) substrate by using ion-beam sputter deposition. The as-deposited Cu-based electrode exhibited much low resistivity (2.7 $\mu\Omega$·cm) than the bulk resistivity of platinum (10.7 $\mu\Omega$·cm), which may greatly reduce the RC constant and boost the switching speed of the BST thin film devices for high-frequency application. To understand Cu diffusion and oxidation

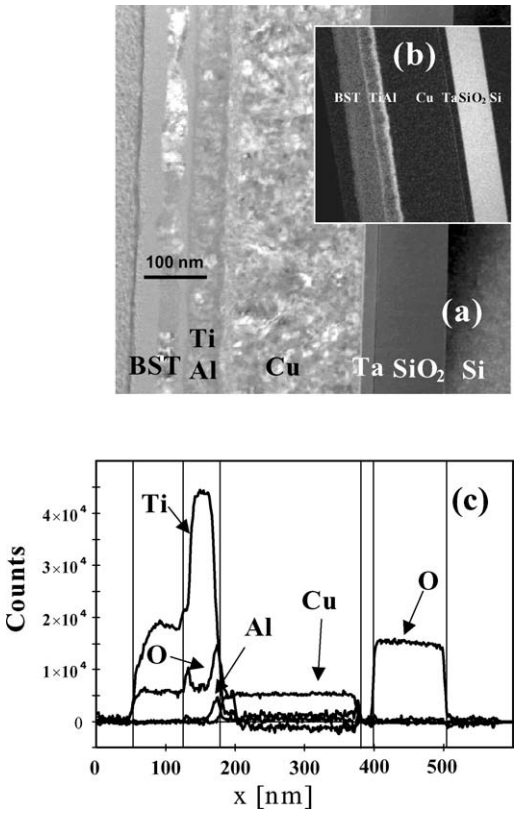


*Fig. 13.* (a) Cross-sectional STEM bright field image, (b) O-K map of BST/TiAl/Cu/Ta sample, and (c) line-scan of Al, Ti, Cu, and O element distribution across the layer, showing that Cu layer is free of oxygen and is well confined within the TiAl and Ta barriers.

mechanism and to develop materials integration strategies for producing a reliable Cu-based electrode technology for high-k capacitors, TiAl/Cu/Ta structures were heated up to 600°C in conventional furnace filled with constant flow of 99.9% oxygen. Electrical measurement, XPS depth profile, RBS, and XRD analyses revealed that the layered Cu-based electrode was able to maintain its low electrical resistivity (2.7 $\mu\Omega$·cm) and structure integrity in oxygen up to 600°C. BST thin films were deposited on the Cu-based electrodes substrates by radio-frequency magnetron sputter deposition at temperature from 400 to 600°C in an mixture of $O_2$ and Ar (1:5). For the first time, polycrystalline BST thin films with perovskite structure were obtained on Cu electrode, using TiAl and Ta as barriers. The layered BST/TiAl/Cu/Ta/$SiO_2$/Si structure with a very smooth BST surface was studied using cross-sectional SEM and TEM. No interdiffusion was detected in the sample grown at $\leq$500°C.

### 6.2. *Composition and Microstructural Characterization of Layered Cu-Based Electrodes*

Figure 13(a) shows a STEM bright-field image of a cross-section BST/Cu-based electrode sample, while Fig. 13(c) shows line-scans of the elements Al, Ti, O and Cu measured across all the layers. These line-scans were derived from elemental maps calculated from energy-filtered TEM images using the three-window-method [25]. The imbedded image (Fig. 13(b)) gives an example of O-K map. The pixel-size of these images is 1.2 nm and the CCD-camera was operated with 2× binning. The intensity was integrated for a line-scan width of 10 pixels to improve the signal-to-noise ratio. The width of the energy selection aperture used for recording the individual energy filtered images was 10 eV for the Ti-$L_{23}$ edge, O-K edge, and Cu-$L_{23}$ edge and 30 eV for the Al-K edge. These line-scans across all layers show steep concentration

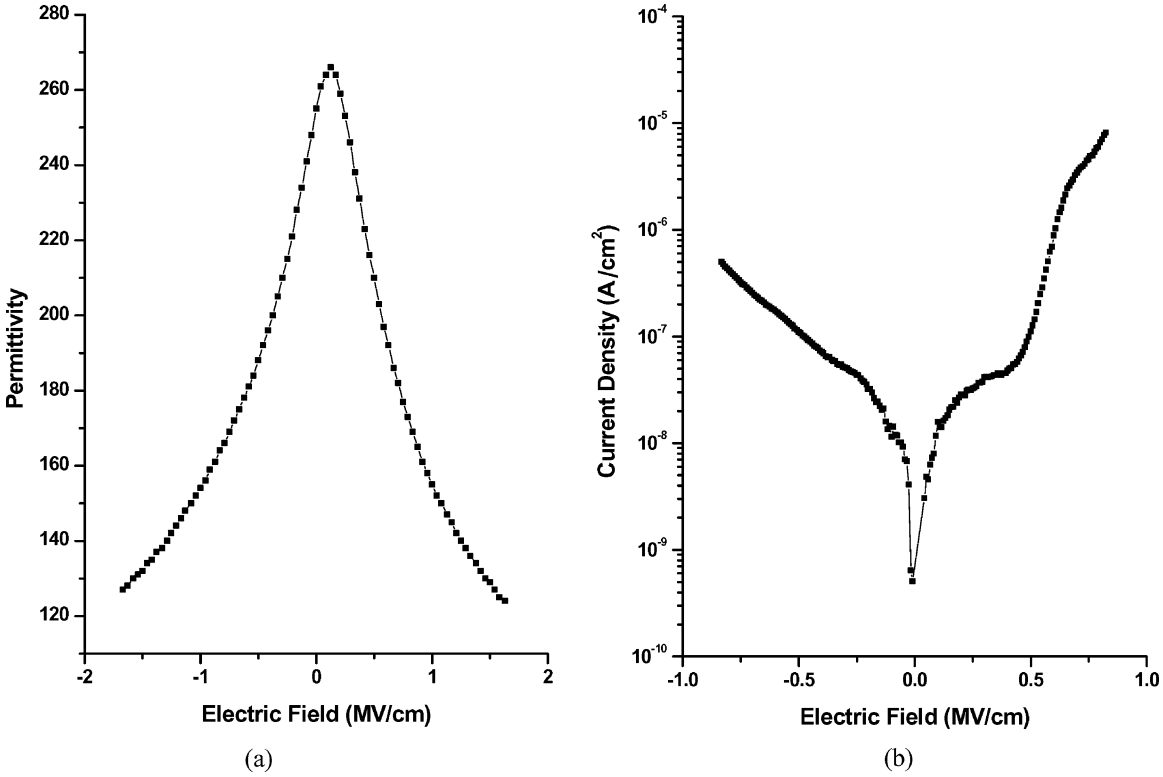


(a) (b)

*Fig. 14.* (a) C–V and (b) I–V curves of BST thin film deposited at 450°C followed by 2-min RTA.

gradients at the interfaces with a width of only a few nanometers. Very low oxygen level has been detected within the Cu layer and practically no Cu atom diffused into Si substrate, which indicate the excellent barrier properties of TiAl and Ta.

The optimized process for fabrication of BST thin film capacitors with Cu-based electrode involves sputter deposition of BST thin films at 400 to 450°C followed by 2-min rapid thermal annealing (RTA) at 700°C in oxygen atmosphere [26]. With this method, the low-$k$ interfacial layer formed between BST and TiAl barrier and interface roughening caused by Cu-recrystallization at high temperature can be greatly suppressed. As the result, large dielectric constant, $\varepsilon_r = 280$, and low dielectric loss, $\tan\delta = 0.007$, were achieved for BST capacitors with bottom Cu-based electrodes. The dielectric constant of the 160-nm BST layer as a function of applied electric field is plotted in Fig. 14(a). The positive and negative signs of the field were decided by the voltage applied on the Pt (top-electrode) with respect to the TiAl/Cu/Ta (bottom-electrode). The field-dependent permittivity shown in Fig. 14(a) indicates a tunability of 53%. Figure 14(b) shows the leakage current density as a function of the applied electric field. The asymmetric shape of the I-V curve is primarily due to the asymmetric electrode structure using Pt at top and TiAl at bottom. Leakage below $2 \times 10^{-8}$ A/cm$^2$ at 100 kV/cm was achieved with a breakdown field of 450 kV/cm.

## 7. Conclusions

In conclusion, we have shown that solid solution and multi-layered BST films with high tunabilities, low losses, and high dielectric breakdown fields can be synthesized using RF-magnetron sputter deposition with judiciously chosen process parameters. Specifically, control is demonstrated of the composition (i.e., the (Ba + Sr)/Ti ratio) of BST films grown from a single stoichiometric target by use of tailored target-substrate geometry and deposition pressure. MOCVD BST films were also grown to demonstrate the capability of producing very good quality large area films which show excellent electrical properties. The issues related to interface contamination have been touched upon, where we demonstrated that post top electrode deposition annealing treatments can lead to large improvement in electrical properties of the BST films, specifically reducing loss and leakage current. The improvements in the electrical properties have been attributed to the elimination of C, H impurities from electrode/BST interface through a thermal annealing process.

Periodically loaded line phase shifters with up to 160° of phase shift at 30 GHz were fabricated by York et al. using BST films produced in our program. The phase shift increased linearly with frequency as expected for a variable time delay element. The phase shifters produced by using our BST films are not fully optimized yet. However, the result presented in this paper indicate the potential of thin film BST technology for high frequency devices.

A successful attempt was made to replace Pt with Cu as the bottom electrode for BST films. To overcome the problems of Cu integration with high-k oxides, we have investigated the oxidation and diffusion resistance of TiAl/Cu/Ta multilayered structure, which showed high electrical conductance and excellent thermal stability in oxygen environment up to 600°C. The electrical properties of these heterostructured films show good electrical properties, while further work is being pursued towards improvements of the film properties and successful integration into microwave and other potential devices.

## Acknowledgments

This work was supported by the U.S. Department of Energy, FreedomCAR and Vehicle Technologies Program and Basic Energy Sciences—Materials Sciences under contract W-31-109-ENG-38, and by the DARPA-FAME program. The authors would like to acknowledge the contributions of Prof. R. York's group within the DARPA-FAME program, particularly on the integration of ANL thin films into high quality devices designed and fabricated at UCSB.

## References

1. D. Flaviis, N.G. Alexopolous, and M. Staffsudd, *IEEE Trans. Microwave. Tech.*, **45**, 963 (1997).
2. V.K. Varadan, D.K. Ghodgaonker, V.V. Varadan, J.F. Kelly, and
3. P. Glikerdas, *Microwave Journal*, **35**, 116 (1992).
4. J.M. Ponds, S.W. Kirchoefer, W. Chang, J.S. Horwitz, and D.B. Chrisey, *Integr. Ferroelectr.*, **22**, 317 (1998).
5. F.A. Miranda, F.W. Van Keuls, R.R. Romanofsky, and G. Subramanyam, *Integr. Ferroelectr.*, **22**, 269 (1998).
6. A.I. Kingon, S.K. Streiffer, C. Basceri, and S.R. Summerfelt, *MRS Bull.*, **21**, 18 (1995).

7. J. Im, O. Auciello, P.K. Baumann, S.K. Streiffer, D.K. Kaufman, and A.R. Krauss, *Appl. Phys. Lett.*, **76**, 625 (2000).
8. P.K. Baumann, D.Y. Kaufman, J. Im, O. Auciello, S.K. Streiffer, R.A. Erck, and J. Giumarra, *Integrated Ferroelectrics*, **34**, 255 (2001).
9. G.W. Dietz, M. Schumacher, R. Waser, S.K. Streiffer, C. Basceri, and A.I. Kingon, *J. Appl. Phys.*, **82**, 2359 (1997).
10. C. Basceri, S.K. Streiffer, A.I. Kingon, and R. Waser, *J. Appl. Phys.*, **82**, 2497 (1997).
11. S.K. Streiffer, C.Basceri, C.B. Parker, S.E. Las, and A.I. Kingon, *J. Appl. Phys.*, **86**, 4565 (1999).
12. S. Saha, D.Y. Kaufman, S.K. Streiffer, and O. Auciello, *Appl. Phys. Lett.*, **83**, 1414 (2003).
13. O. Auciello, A.R. Krauss, J. Im, and J.A. Schultz, *Annu. Rev. Mater. Sci*., edited by O. Auciello and R. Ramesh, vol. **28** (1998), p. 375.
14. J. Im, A.R. Krauss, Y. Lin, J.A. Schultz, O. Auciello, D.M. Gruen, and R.P.H. Chang, *Nucl. Instrum. Meth.*, **B118**, 772 (1996).
15. P. Padmini, T.R. Taylor, M.J. Lefevre, A.S. Nagra, J.S. Speck, and R.A. York, *Appl. Phys. Lett.*, **75**, 3186 (1999).
16. A. Nagra, T.R. Taylor, P. Periaswamy, J.S. Speck, and R.A. York, *MRS Symp. Proc.*: "Materials Issues for Tunable RF and Microwave Devices", vol. 603 (2000) p. 37.
17. R. York, A. Nagra, P. Periaswamy, O. Auciello, S.K. Streiffer, and J. Im, *Integrated Ferroelectrics*, **34**, 177 (2001).
18. H. Takasago, K. Adachi, and M. Takada, *J. Electron Mater.*, **12**, 319 (1989).
19. J. Li, G. Vizekelethy, P. Revez, J.W. Mayer, and K.N. Tu, *J. Appl. Phys.*, **69**, 1020 (1991).
20. W. Fan, S. Saha, J.A. Carlisle, O. Auciello, R.P.H. Chang, and R. Ramesh, *Appl. Phys. Lett.*, **82**, 1452 (2003).
21. K. Holloway, P.M. Fryer, C. Cabral, Jr., J.M.E. Harper, and P.J. Bailey, *J. Appl. Phys.*, **71**, 5433 (1992).
22. P. Catania, J.P. Doyle, and J.J. Cuomo, *J. Vac. Sci. Technol.*, **A10**, 3318 (1992).
23. S. Aggarwal, A.M. Dhote, H. Li, S. Ankem, and R. Ramesh, *Appl. Phys. Lett.*, **74**, 230 (1999).
24. A.M. Dhote, O. Auciello, D.M. Gruen, and R. Ramesh, *Appl. Phys. Lett.*, **79**, 800 (2001).
25. L. Reimer (ed.), *Energy-Filtering Transmission Electron Microscopy*, (Springer, Berlin, Heidelberg, 1995), p. 382.
26. W. Fan, B. Kabius, J.M. Hiller, S. Saha, J.A. Carlisle, O. Auciello, R.P.H. Chang, and R. Ramesh, *J. Appl. Lett.*, **94** (Nov. 15, 2003).